

Spin flip locking by the tunneling and relaxation in a driven double quantum dot with spin-orbit coupling

D.V. Khomitsky,^{1,*} M.V. Bastrakova,^{1,2} and D.S. Pashin¹

¹*Department of Physics, National Research Lobachevsky State University of Nizhny Novgorod, 603022 Gagarin Avenue 23, Nizhny Novgorod, Russian Federation*

²*Russian Quantum Center, 143025 Skolkovo, Moscow, Russian Federation*

(Dated: November 28, 2024)

Coupled spin evolution and tunneling together with the relaxation and decoherence effects are studied for the double quantum dot formed in a semiconductor nanowire and driven by the periodic electric field. Such system represents a model of the spin and charge qubits interacting via the strong spin-orbit coupling. It is found that at certain regimes the combination of fast relaxation in the coordinate channel with the slower relaxation in the spin channel leads to the promising combination of fast spin manipulation and slow spin relaxation, locking the flipped spin in an excited state in one of the dots for a sufficiently long time. The predicted effect is maintained for a wide range of the relaxation times and the driving amplitude both for the coordinate and the spin channels and is also observed on higher subharmonic which requires lower driving frequencies.

I. INTRODUCTION

The spin dynamics in low dimensional semiconductor structures demonstrates a great variety of both fundamental phenomena and promising applications in spintronics and quantum computations. The basic building block representing the qubit, i.e. the two-level system, has been the subject of intensive research where different phenomena such as the Landau-Zener-Stückelberg-Majorana (LZSM) interference^{1,2} have been studied. The coupled tunneling and the spin evolution in semiconductor structures with quantum dots have been the subject of intensive research³⁻¹³ including the experimentally observed manifestation of the interplay between the tunneling and the spin flip associated with the electric dipole spin resonance (EDSR) and its subharmonics in the gate-defined single and double quantum dots (QD) in semiconductor structures¹⁴⁻²⁴. Such systems may represent a model of the hybrid spin-charge qubit²⁵⁻³³ where the Zeeman splitting generates the two-level subspace of the spin subsystem and the double or multi-dot³⁴ confinement potential provides a controlled charge distribution for the two-level charge (coordinate) subspace encoding the states by the electron location in left- or right-QD. The two qubits may interact via the spin-orbit coupling intrinsically present in the given structure or generated by the non-uniform magnetic field³⁵ and driven by the monochromatic or two-photon Raman³⁶ mechanism.

Motivated by the mentioned experiments, we have studied in our recent papers^{37,38} the LZSM effects for the coupled spin and charge dynamics driven in the double quantum dots by the periodic electric field and the spin-orbit coupling (SOC), focusing on the EDSR³⁷ and its subharmonics³⁸. It was found that the tunneling may enhance the SOC-induced spin flip via the interdot tunneling. The effects studied in these papers has been considered on relatively short time scales which allowed to neglect the relaxation effects and to consider only the coherent dynamics.

When several, at least two interacting quantum dots (or qubits) are considered on the time interval comparable with the relaxation time in any of the subsystems, the enlarged size of the structure and the associated transport and tunneling effects inevitably call for the consideration of various relaxation and decoherence effects studied under the well-known density matrix formalism³⁹⁻⁴⁴. The applications include the already mentioned low dimensional semiconductor structures with quantum dots^{3-7,9,12,13}, the qubits based on the Josephson junctions⁴⁵⁻⁴⁸, the circuit or cavity quantum electrodynamics^{49,50}, the entangled photons⁵¹, the three-level systems⁵², and many others. The primary question is how well the results obtained within the coherent dynamics approximation survive on the specific time intervals and what qualitatively new effects the relaxation and decoherence may introduce into the coupled tunneling and spin dynamics in addition to the trivial damping and smearing of the valuable signals.

In this paper we include the relaxation and decoherence within the master equation approach for the electron density matrix and study the driven spin dynamics coupled with the interdot tunneling in a double quantum dot under the periodic driving by the electric field. Similar to our previous studies^{37,38}, we consider the resonant spin-flip transitions assisted by the interdot tunneling. It is found that under some circumstances the relaxation can play an unexpectedly stabilizing role for the spin flip, locking the flipped spin in the excited Zeeman state. The mechanism is activated in the resonant regime where the spin flip is accompanied with the interdot tunneling. The fast charge relaxation drives the electron into the single dot having the lower energy for the charge degree of freedom while the spin maintains its flipped state on the longer time scale which may go beyond the spin relaxation time due to the driving. This effect, similar to the ones observed in three-level atomic and laser systems⁵³⁻⁵⁵ but observed mainly in the GH_z frequency range in the semiconductor dot experiments²⁰⁻²⁴, can be

observed for various system parameters and both on the main and the sub-harmonics of the resonance, is of fundamental interest and is promising for the spin manipulation technique development in nanostructures. Our predictions may stimulate the development of coupled spin and charge qubit setups where the charge dynamics improves the characteristics of the spin evolution.

This paper is organized as follows. In Sec. II we describe the Hamiltonian and its lowest four-level subspace forming the coupled spin and charge qubits. The degree of the validity for the four-level model for the coherent dynamics is evaluated by searching for the borders in the parameter space which enclose the impact of the four lowest levels above the preset threshold. We extend the approach by introducing the evolution equation for the electron density matrix with the Lindblad operators and the relaxation rates for the charge and spin two-level subsystems, respectively. In Sec. III we present the numerical analysis of the regimes where the spin flip is assisted by the interdot tunneling and visualize the spin evolution on the associated Bloch sphere for each qubit subsystem. We consider different types of resonances both without and with the interdot tunneling. In the regime with the interdot tunneling, we observe the unexpectedly stabilizing role of the relaxation at certain regimes on the spin flip in a single dot where the electron has been initialized in the ground state. Finally, in Sec. IV we give our conclusions.

II. MODEL

A. The Hamiltonian

The Hamiltonian which we use describes the single-particle states in a double quantum dot formed in a semiconductor nanowire by the gate potential. It has been derived and studied in detail in our preceding papers^{37,38}. It is expressed via the sum

$$H(t) = H_0 + V_d(t), \quad (1)$$

where the time-independent part of the Hamiltonian H_0 is

$$H_0 = H_{2QD} + H_Z + H_{SO}. \quad (2)$$

In (2) the contribution H_{2QD} corresponds to the movement of the electron in the double-minima potential of the quantum dot with the detuning,

$$H_{2QD} = k_x^2/2m + U_0(x) + U_d f_1(x). \quad (3)$$

Here m is the effective mass in the lowest subband of the size quantization in the nanowire (we use the units with $\hbar = 1$). The double-minima potential is modeled

by the function $U_0(x) = U_0((x/d)^4 - 2(x/d)^2)$, where $2d$ is the interdot center distance and U_0 is the interdot barrier height. The last term $U_d f_1(x)$ in (3) describes the static detuning being the difference between the interdot minima. Here the function $f_1 = (x/d_1)^3 - 3/2 \cdot (x/d_1)^2$ models the smooth connection with the initial double well potential with $d_1 = 1.5d$ and provides the bottom-down shift for the right QD at $U_d < 0$.

The second term in (2) is the Zeeman coupling

$$H_Z = \frac{1}{2} g \mu_B B_z \sigma_z \quad (4)$$

generated by the static magnetic field which is the direction of the Oz axis, and g is the effective g -factor, controlling the Zeeman splitting being the characteristic energy scale of the spin subsystem

$$\Delta_1 = g \mu_B B_z. \quad (5)$$

We may call the Zeeman-split pair of states (\downarrow, \uparrow) in each dot as the spin subsystem (or spin qubit) with the distance between the levels Δ_1 shown on the left panel of Fig.1.

We will label the eigenstates and the energy levels of the coordinate part of the double dot Hamiltonian (3) as $\phi_n(x)$ and ε_n , respectively. The interdot minima splitting is the characteristic splitting Δ_2 for the charge subsystem,

$$\Delta_2 = \varepsilon_2 - \varepsilon_1, \quad (6)$$

where the numerical calculation of the energy levels gives us $\Delta_2 = \gamma |U_d|$ with $\gamma \approx 0.55$. For the negative detuning $U_d < 0$ with $|U_d| \ll U_0$ the ground state ε_1 with the wavefunction $\phi_1(x)$ is located in the right QD with the exponentially small overlap with the left QD and the next state $\phi_2(x)$ is located in the left QD. This makes the basis for the charge two-level subsystem by attributing the wavefunction location to the right and left QD, respectively. If we restrict ourselves to this two-level subspace for the coordinate degree of freedom we may call it as representation of a charge qubit which is shown schematically on the right panel in Fig.1.

The spin and charge qubits are coupled via the third term in (2) which is the SOC that may contain both Dresselhaus and Rashba terms. Here we will limit ourselves to the Dresselhaus term only since the Rashba term provides similar impact on the spin and charge evolution³⁸. For the leading order in the wavevector the SOC is linear for the GaAs-based nanowire,

$$H_{SO} = \beta_D \sigma_x k_x, \quad (7)$$

where β_D is the strength of the Dresselhaus term. We perform the numerical diagonalization of the static Hamiltonian (2),

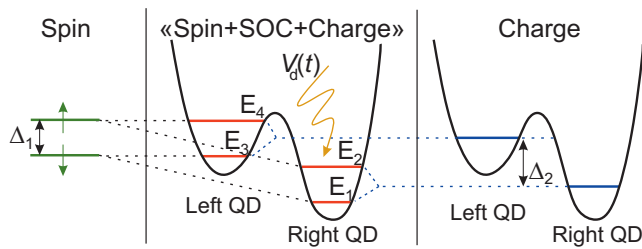


FIG. 1. Scheme of the spin (left) and charge (right) qubits in a double quantum dot with the lowest subspace of the levels E_1, \dots, E_4 of the coupled spin-charge qubit (center). The splitting Δ_1 for the spin qubit is generated by the Zeeman term (5), the splitting Δ_2 for the charge qubit is generated by the detuning which shifts the relative position of the dot energy minimum. The two qubits are coupled via SOC and driven by the periodic electric field $V_d(t)$.

$$H_0\Psi_n = E_n\Psi_n, \quad (8)$$

and obtain the set of energy levels E_n and the two-component eigenfunctions $\Psi_n(x)$. The principal scheme for the lowest four-level subspace in (8) describing the two coupled spin and charge qubits is given in the center panel of Fig.1 for the negative detuning $U_d < 0$. In this basic example the level pairs (E_1, E_2) as well as (E_3, E_4) represent the spin qubit with the splittings in each dot

$$E_2 - E_1 = \Delta_1^{(1)}, \quad E_4 - E_3 = \Delta_1^{(2)}, \quad (9)$$

which are slightly different from each other and from the Zeeman splitting Δ_1 from (5) due to the corrections from the SOC term (7). The level pairs (E_1, E_3) and (E_2, E_4) belonging to the neighboring dots represent the charge qubit with the splitting

$$E_3 - E_1 = \Delta_2^{(1)}, \quad E_4 - E_2 = \Delta_2^{(2)}, \quad (10)$$

where again due to SOC the splittings $\Delta_2^{(1,2)}$ are slightly different from the spinless level splitting Δ_2 defined in (6). It should be noted that due to the presence of the SOC the amplitude of the z -projection of the spin along the direction of the magnetic field for an eigenstate of the Hamiltonian (2) is always less than 1. It means that these eigenstates in (8) are not pure spin-up or spin-down states, although for the chosen parameters their in-plane spin projection is sufficiently smaller (about 1% in magnitude) than the z -projection. This allows us the consideration of the spin-split states in each QD as the states of the single spin subsystem (spin qubit) similar to the pure Zeeman-split states (\downarrow, \uparrow).

The second term in (1) is the periodic driving with the amplitude V_d , generating the time-periodic potential

$$V_d(t) = V_d \sin \omega t f_2(x). \quad (11)$$

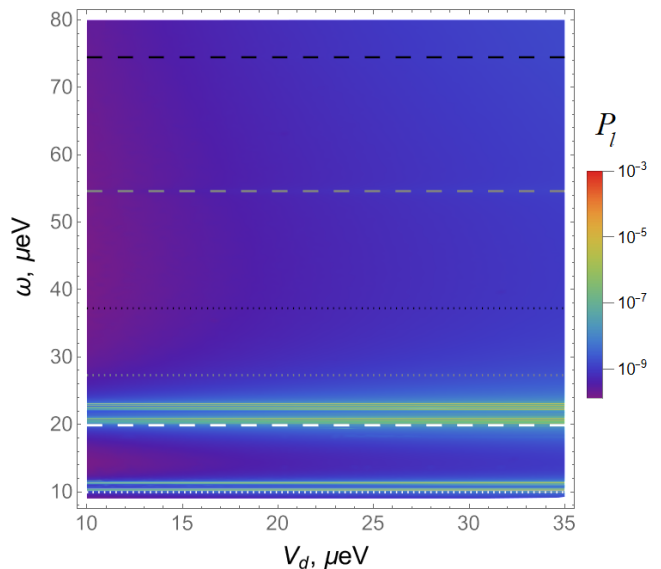


FIG. 2. Contour plots of the leakage probability (13) in the plane of the driving field parameters (V_d, ω) describing the impact on the evolution produced by the higher levels above the lowest four-level subspace in Fig.1 after $N = 5000$ periods of the driving field. The black, grey and white dashed lines indicate the resonance transitions between the levels $E_1 - E_4$, $E_1 - E_3$ and $E_1 - E_2$ in Fig.1 for the splitting $\Delta_1 = 20\mu eV$ and $\Delta_2 = 55\mu eV$, and the dotted lines of the same colors indicate their second subharmonics. About $10^{-8} \dots 10^{-7}$ of the leakage probability P_l is observed along the line $\omega \sim 20\mu eV$ during the hybridization of the $E_1 - E_2$ level resonance and the high subharmonic of the $E_1 - E_5$ resonance, as well for the other operating frequencies.

This potential describes the gate-defined electric field which is focused on the right QD only, modeled by the Gaussian shape $f_2(x) = \exp(-(x-d)^2/2d^2)$. Below the system evolution is studied in the basis of the states (8) with the driving (11).

B. Four-level approximation

First, we will take a look on the coherent driven dynamics without the relaxation in order to determine the regions in the parameter space where the four-level approximation is valid with the preset tolerance which is needful for the model of two coupled qubits described above. The usual solution for the time-dependent Schrödinger equation $i\partial\psi/\partial t = H\psi$ with the Hamiltonian (1) is found as a sum of the eigenfunctions from (8) with time-dependent coefficients^{37,38}:

$$\psi(x, t) = \sum_n C_n(t)\Psi_n(x). \quad (12)$$

To quantify the contribution from the higher levels above our basic four-level subspace, we will define the leakage probability to the higher levels

$$P_l = \max_t \left(1 - \sum_{i=1}^4 |C_i(t)|^2 \right) \quad (13)$$

showing the maximum leakage over the whole evolution time. The most instructive application of (13) is on the map of the parameters describing the driving field, i.e. on the (V_d, ω) plane. In Fig.2 we show the contour plots of (13) after $N = 5000$ periods of the driving field $T = 2\pi/\omega$ for the typical system parameters which include the electron effective mass in the lowest subband $m = 0.11m_0$ where m_0 is the free electron mass, the interdot minima distance $2d = 116 \text{ nm}$ and the interdot barrier $U_0 = 4 \text{ meV}$ for the double dot potential in (3). The driving strength V_d in Fig.2 varies between 10 and 35 μeV which for the typical interdot barrier height $U_0 = 4 \text{ meV}$ ^{37,38} gives the ratio $V_d/U_0 = 0.0025 \dots 0.0087$, indicating that the interdot barrier shape is only weakly disturbed by the driving. The distance between the lowest four-level manifold and the next level E_5 (not shown in Fig.1) for such conditions is $\sim 2000\mu\text{eV}$ which is an order of magnitude greater than the highest energy scale for the lowest four-level subspace and the driving in our model. The Dresselhaus amplitude in (7) is $\beta_D = 3\text{meV} \cdot \text{nm}$. The other system parameters are the following: the detuning $U_d = -100\mu\text{eV}$ corresponding to the level splitting (6) $\Delta_2 = 55\mu\text{eV}$ and the Zeeman splitting $\Delta_1 = 20\mu\text{eV}$. Such Zeeman splitting corresponds to the driving frequency $\sim 5 \text{ GHz}$ which is within the frequency bands used in the experiments²². The initial state for the evolution is the ground state E_1 in Fig.1 which for the taken parameters is the spin-down state in the right QD.

In Fig.2 the black, grey and white dashed lines indicate the resonance transitions between the levels $E_1 - E_4$, $E_1 - E_3$ and $E_1 - E_2$ in Fig.1 for the energy splitting parameters in (5) and (6) taken as $\Delta_1 = 20\mu\text{eV}$ and $\Delta_2 = 55\mu\text{eV}$, and the dotted lines of the same colors indicate their second subharmonics. From Fig.2 one can observe the leakage probability of $10^{-8} \dots 10^{-7}$ for all operating frequencies in our modeling which provides a good justification of working within the lowest four-level subspace for the most parts of the parameter map.

A remarkable feature in Fig.2 is that the leakage probability is enhanced at certain frequencies, i.e. on some horizontal lines in Fig.2 where an obvious increase is seen also with the growing driving amplitude. These frequencies, grouped at $\omega \sim 20\mu\text{eV}$ being the spin qubit splitting (9), correspond to the hybridization of the $E_1 - E_2$ level resonance and the high ($k \sim 100$) subharmonic of the $E_1 - E_5$ resonance with the interlevel distance $E_5 - E_1 \sim 2000\mu\text{eV}$. Such amplification of the resonance at the hybridization points in the parameter space have been observed in our preceding paper³⁸. We can draw a conclusion that operating on the basic EDSR frequency $\omega = E_2 - E_1$ seems to be not the best option due to the intensified leakage to the higher levels above the four-level manifold. A better way off flipping the spin

can be the operations on the $E_1 - E_4$ resonance or its subharmonic labeled by the black dashed and dotted lines in Fig.2, respectively. We will gather more justifications on this choice in the next Section.

C. Two-qubit representation

As it can be seen from Fig.2, most of the driving field parameter plane provides a good background for the modeling the evolution within the four-level ground subspace E_1, \dots, E_4 illustrated by Fig.1 which is spanned by the wavefunctions Ψ_1, \dots, Ψ_4 obtained from (8). We will consider them as the states for the two-qubit representation of our system, the first qubit being the spin qubit on the pair of levels $E_1 - E_2$ or $E_3 - E_4$ with the level spacing (9) and the second qubit is the charge qubit on the levels $E_1 - E_3$ or $E_2 - E_4$ with the level spacing (10) provided by the detuning. The two qubits interact via the SOC (7) and are both driven by the periodic field (11).

The description of the Hamiltonian for the two interacting qubits can be made in terms of the Pauli matrices $\sigma_k^{(q)}$, $k = 0, \dots, 3$, attributed to each of the spin ($q = 1$) and charge ($q = 2$) qubits:

$$H_{4 \times 4} = c_{00} \cdot \sigma_0^{(1)} \otimes \sigma_0^{(2)} + c_{03} \cdot \sigma_0^{(1)} \otimes \sigma_3^{(2)} + c_{30} \cdot \sigma_3^{(1)} \otimes \sigma_0^{(2)} + c_{33} \cdot \sigma_3^{(1)} \otimes \sigma_3^{(2)} + F_{4 \times 4} V_d \sin(\omega t). \quad (14)$$

In (14) the coefficients c_{ij} are expressed via the energies E_n from the stationary Schrödinger equation (8) as

$$\begin{aligned} c_{00} &= \frac{E_1 + E_2 + E_3 + E_4}{4}, \\ c_{03} &= \frac{-E_1 - E_2 + E_3 + E_4}{4}, \\ c_{30} &= \frac{-E_1 + E_2 - E_3 + E_4}{4}, \\ c_{33} &= \frac{E_1 - E_2 - E_3 + E_4}{4}. \end{aligned} \quad (15)$$

The first coefficient c_{00} corresponds to the shift of the energy zero and does not affect the system dynamics. The coefficient $2c_{03} = (\Delta_2^{(1)} + \Delta_2^{(2)})/2$ is the averaged distance from (10) between the levels of the charge qubit. The coefficient $2c_{30} = (\Delta_1^{(1)} + \Delta_1^{(2)})/2$ is the averaged Zeeman splitting from (9) slightly corrected by the presence of SOC. The last coefficient c_{33} is zero for the case of the equal Zeeman splittings in the left and right QDs and its nonzero value reflects the slight difference between the spin splitting in two dots created by the combination of SOC and detuning. This coefficient reflects the SOC-induced interaction between the spin and charge subsystems and in our modeling has a typical amplitude $|c_{33}| \sim 10^{-4} \mu\text{eV}$ which allows treating SOC as a perturbation while keeping the concept of the spin and charge

two-level subsystems, each described by its own relaxation parameters studied in the next Subsection. The last term $F_{4 \times 4}$ in (14) is given by the decomposition of the operator $I_{2 \times 2}^{(1)} \otimes f_2(x)$, where $I_{2 \times 2}^{(1)}$ is 2×2 identity matrix in the subspace of the spin qubit, and essentially depends on the shape of the driving function $f_2(x)$, creating in general the matrix $F_{4 \times 4}$ with all non-zero elements. The notation (14) allows us to apply the standard technique of the density matrix formalism for the evolution of the system of two coupled qubits described in the next Section.

D. Evolution of the density matrix

Since we are interested in the evolution modeling on different time scales including the ones comparable with the relaxation times, we will include the relaxation and decoherence for our system via the density matrix approach. We suppose that each of the spin and charge qubits interacts with its corresponding thermostat independently and is described by the specific phase and energy dissipators and the relaxation rates $\Gamma_\varphi^{(q)}$, $\Gamma_e^{(q)}$ for the spin and charge subsystems, providing the additive impacts into the global system dissipator^{56,57}. The full two-qubit density matrix describes the evolution of two coupled qubits governed by the equation written in the Lindblad form in the instant (adiabatic) basis^{2,45,47}:

$$\begin{aligned} \frac{\partial \rho}{\partial t} &= -i[H_{4 \times 4}, \rho] + \Gamma \rho, \\ \Gamma &\equiv \sum_{q=1}^2 \left(\frac{\Gamma_\varphi^{(q)}}{2} D[\bar{\sigma}_3^{(q)}] + \Gamma_e^{(q)} D[\bar{\sigma}_-^{(q)}] \right), \end{aligned} \quad (16)$$

where the dash over the Pauli matrices indicates that they are written in the adiabatic basis. In Eq.(16) the Hamiltonian $H_{4 \times 4}$ from (14) is described in the previous Subsection, and the Lindblad operators are given by

$$\begin{aligned} D[a]\rho &\equiv a \rho a^\dagger - \frac{1}{2} \{a^\dagger a, \rho\}, \\ \bar{\sigma}_-^{(q)} &\equiv \frac{1}{2} (\bar{\sigma}_1^{(q)} - i \bar{\sigma}_2^{(q)}). \end{aligned} \quad (17)$$

We consider the approximation where each of the spin and charge subsystems interacts with its own dominating source of relaxation. For the GaAs double dots it can be the interaction with the nuclear spins for the spin subsystem and the interaction with the structural defects and phonons for the charge subsystem. Such approximation allows treating their reservoir parameters separately, introducing the phase and energy relaxation rates $\Gamma_\varphi^{(q)}$ and $\Gamma_e^{(q)}$ for each qubit subsystem ($q = 1, 2$) as follows⁴⁵:

$$\Gamma_\varphi^{(q)} = \pi \alpha^{(q)} 2k_B \tau \cos^2 \eta^{(q)},$$

$$\Gamma_e^{(q)} = \pi \alpha^{(q)} \Delta \bar{E}^{(q)} \coth \frac{\Delta \bar{E}^{(q)}}{2k_B \tau} \sin^2 \eta^{(q)}. \quad (18)$$

It should be mentioned that the energy relaxation rates in Eq.(18) are energy-dependent, i.e. they vary with the inter-level distance $\Delta \bar{E}^{(q)}$ for the adiabatic basis. In Eq.(18) k_B and τ are the Boltzmann constant and the thermostat temperature, and the parameters $\eta^{(q)}$ and $\alpha^{(q)}$ describe the subsystem-thermostat coupling type and strength, respectively. For convenience in what follows we will use the characteristic relaxation times defined via (18) at the initial moment $t = 0$: $T_\varphi^{(q)} = 2\pi/\Gamma_\varphi^{(q)}(0)$ and $T_e^{(q)} = 2\pi/\Gamma_e^{(q)}(0)$. The energy parameters $\Delta \bar{E}^{(q)}$ describe the inter-level distance in the instant basis,

$$\begin{aligned} \Delta \bar{E}^{(1)} &= 2\bar{\epsilon}_{30}(t), \\ \Delta \bar{E}^{(2)} &= 2\bar{\epsilon}_{03}(t), \end{aligned} \quad (19)$$

where $\bar{\epsilon}_{ij}(t)$ can be found from (15) by the formal replacement of the energies E_i for the stationary part of the Hamiltonian in (8) by the instant basis energies $E_i(t)$ which can be found from the equation

$$H(t)\Psi_i(t) = E_i(t)\Psi_i(t), \quad (20)$$

where $H(t)$ is the time-dependent Hamiltonian (1). It should be mentioned that the validity of Eq.(16) is justified if the adiabaticity condition⁵⁸ is satisfied:

$$h/\delta^2 \ll 1, \quad (21)$$

where

$$\delta = \min_{t,n,m} |E_n(t) - E_m(t)| \quad \text{and} \quad (22)$$

$$h = \max_{t,n,m} |\langle \psi_n(t) | \partial_t H(t) | \psi_m(t) \rangle|. \quad (23)$$

Our calculations show that the typical value of the adiabaticity parameter h/δ^2 in (21) is $\sim 0.02 \dots 0.07$ which justifies the evolution equation in the form of Eq.(16).

After solving Eq.(16) for the given parameters of the qubit subsystems and the driving in Eq.(14) we calculate the average values tracking the evolution of the each subsystem: the spin projections $\langle \sigma_{x,y,z} \rangle(t)$ tracking the state of the spin qubit where we are mainly interested in the evolution of the z -projection of the spin, and the electron position $\langle x/d \rangle(t)$ tracking the state of the charge qubit.

III. NUMERICAL RESULTS

A. EDSR affected by the spin relaxation

We consider a typical double dot formed by electrostatic gates in a GaAs nanowire similar to the ones

used in the experiments²² and modeled in our preceding papers^{37,38}. We begin with the discussion of the relaxation effects on the most basically considered pure EDSR regime. In Fig.3 we show the stroboscopic evolution of the z -projection of the spin $\langle\sigma_z\rangle(t)$ (in units of $\hbar/2$) for the moments of time $t = nT$ where T is the period of the driving field obtained after solving Eq.(16) on 5000 T time interval with the frequency matching the level distance $E_2 - E_1$ (see Fig.1) defined by the Zeeman splitting $\Delta_1 = 20\mu\text{eV}$. The total evolution time is about $1\ \mu\text{s}$. The system parameters are the same as in Subsection II.B and in Fig.2 where we choose the moderate driving amplitude $V_d = 30\ \mu\text{eV}$. On panel (a) the plot is shown vs time measured in microseconds (upper scale) in the driving field period (lower scale). On panel (b) the stroboscopic evolution of all three spin projections representing the spin qubit is shown on its Bloch sphere which can be introduced for both spin and charge qubit separately,

$$\mathbf{S}^{(q)}(t) = \left(\langle\sigma_1^{(q)}\rangle(t), \langle\sigma_2^{(q)}\rangle(t), \langle\sigma_3^{(q)}\rangle(t) \right). \quad (24)$$

Here the spin and charge qubit evolution corresponds to $q = 1$ and $q = 2$ in (24), respectively. The initial state is the ground spin-down state with energy E_1 in the right QD (see Fig.1), being on the south pole of the sphere in Fig.3(b). Black curve shows the coherent evolution when there is no coupling with the thermostat. Blue curve is for the relaxation times $T_\varphi^{(2)} = T_e^{(2)} = 0.4\ \mu\text{s}$. As to the spin relaxation, we consider it to be much longer, $T_\varphi^{(1)} = T_e^{(1)} = 10T_\varphi^{(2)}$. Red curve is for the shorter relaxation times $T_\varphi^{(2)} = T_e^{(2)} = 0.2\ \mu\text{s}$, and again, $T_\varphi^{(1)} = T_e^{(1)} = 10T_\varphi^{(2)}$. The thermostat temperature for the blue and red curves is $\tau = 100\ \text{mK}$. We have considered rather long relaxation times in order to illustrate the evolution on the smaller EDSR frequency in this Subsection (compared to the frequencies in the next Subsection) before they are damped completely.

The analysis of the evolution in Fig.3 indicates that the relaxation provides just the simple damping for the pure two-level spin dynamics at the EDSR if the tunneling is effectively turned off. Several incomplete spin rotations are possible, but the onset of the spin relaxation dampers the spin oscillations after several μs , leading to the need of stronger driving which will reduce the probability of the system to stay within the lowest four-level subspace of the double dot. Thus, we may conclude that another type of the resonance, maybe involving the tunneling in addition of the spin flip, can be of interest for the efficient spin manipulation, which is described in the following Subsection.

B. Spin flip locking by the tunneling and relaxation

We continue with the evolution analysis for another type of the resonance where the spin flip is accompanied

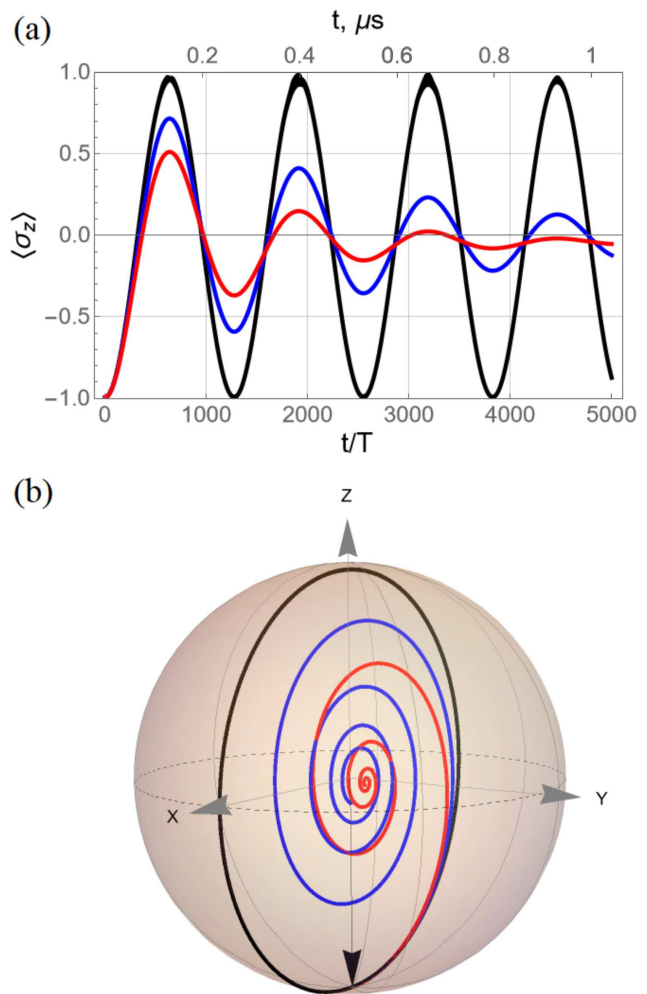


FIG. 3. (a) Stroboscopic evolution of $\langle\sigma_z\rangle(t)$ (in units of $\hbar/2$) for the main EDSR harmonic at the resonance between the levels E_1 and E_2 in Fig.1. Plot is shown vs time (upper scale) and vs the number of driving field periods (lower scale); (b) Stroboscopic evolution of the vector (24) for the spin qubit ($q = 1$) shown on its Bloch sphere. The system parameters are the same as in Fig.2 with the driving frequency defined by the Zeeman splitting $\Delta_1 = 20\mu\text{eV}$ and the amplitude $V_d = 30\ \mu\text{eV}$. The initial state is the ground spin-down state with energy E_1 in the right QD marked by the black downward arrow. Black curve is for the absence of coupling with the thermostat. Blue curve is for the relaxation times $T_\varphi^{(2)} = T_e^{(2)} = 0.4\ \mu\text{s}$, and we take everywhere $T_\varphi^{(1)} = T_e^{(1)} = 10T_\varphi^{(2)}$. Red curve is for $T_\varphi^{(2)} = T_e^{(2)} = 0.2\ \mu\text{s}$. The thermostat temperature in two latter cases $\tau = 100\ \text{mK}$. The relaxation provides trivial damping for pure two-level spin dynamics without tunneling.

by the effective tunneling. This type of resonance corresponds to the pair of levels E_1 and E_4 in Fig.1 where the spin flip is accompanied with the effective interdot tunneling^{37,38}. Here the basic system parameters are the same as in the previous Subsection. The frequency of the resonance between the levels E_1 and E_4 is determined by the sum $\Delta_1 + \Delta_2 = 75\ \mu\text{eV}$ giving us the

linear frequency $f \sim 18 \text{ GHz}$ which is still within the frequency bands used in the experiments²². The characteristic timescale for the developing spin and coordinate dynamics is much faster than in the previous Subsection, it is in between of the charge and spin relaxation timescales which allows to capture well-established spin rotations. One should mention that the amplitude of the driving field $V_d = 30 \mu\text{eV}$ is lower than the detuning amplitude, meaning that we are not in the effective LZSM regime with the level anticrossing^{2,37} but purely in the resonance at $E_4 - E_1 = \omega$. The initial state for the evolution is again the ground state E_1 . The total evolution time for the modeling is about 100 ns which is within the range of the earlier experiments on EDSR-induced current oscillations in GaAs gate-defined double dots where no significant damping has been observed²⁰.

In Fig.4 we show the evolution for the mean values of the spin projection $\langle \sigma_z \rangle(t)$ and the coordinate $\langle x \rangle(t)$, the latter measured in units of d , obtained after solving Eq.(16) on the $2000 T$ with the frequency matching the level distance $E_4 - E_1$ (see Fig.1). The associated evolution on the Bloch sphere of the vector (24) is shown in Fig.5 for (a) spin qubit and (b) charge qubit. The initial state is on the south pole for both qubits. It is clear that for all considered values of the relaxation parameters the evolution on the Bloch sphere is similar for both qubits and can be described as a small-radius rotation around the z axis with the full-scale oscillations between the south and the north poles. The final position of the vector (24) in Fig.5, as it can be concluded from Fig.4, is on the north pole for the spin qubit in panel (a) and on the south pole for the charge qubit in panel (b).

As in the previous Subsection, we consider three sets of the relaxation parameters. For the first set corresponding to the black curves there is no coupling with the thermostat, i.e. it is the basic case of the coherent evolution studied earlier^{37,38}. For the second set corresponding to the blue curves the charge qubit relaxation times $T_\varphi^{(2)} = T_e^{(2)} = 0.4 \mu\text{s}$, and the spin qubit relaxation times are ten times slower, $T_\varphi^{(1)} = T_e^{(1)} = 10T_\varphi^{(2)}$. This is a typical situation in semiconductor nanowires and quantum dots where the spin relaxation is substantially slower than the momentum relaxation. The spin relaxation time in the GaAs-based double dot system with the detuning is expected to be much longer, at least an order of magnitude^{9,10}. For the third set described by the red curves the relaxation is faster, $T_\varphi^{(2)} = T_e^{(2)} = 0.2 \mu\text{s}$, and $T_\varphi^{(1)} = T_e^{(1)} = 10T_\varphi^{(2)}$. The fastest charge relaxation time of 200 ns is of the same order as the maximum evolution time of 700 ns in Fig.4 and is comparable to the coherence time obtained in recent calculations for the double dots with detuning¹². The considered scale of spin and charge relaxation times means that the charge (coordinate) subsystem evolves during the evolution towards its ground state which is the lowest level E_1 in the right QD while the spin subsystem is still far from its ground state. The thermostat temperature for the second and third set

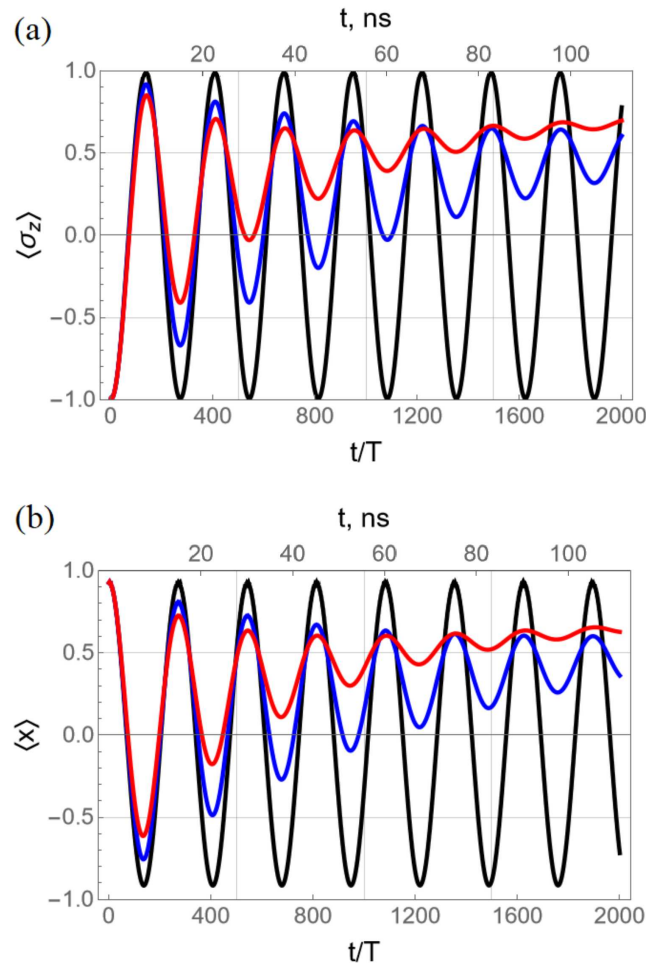


FIG. 4. Evolution of (a) the mean spin projection $\langle \sigma_z \rangle(t)$ and (b) the mean coordinate $\langle x \rangle(t)$ (in units of d) for the spin-flip tunneling resonance between the levels E_1 and E_4 on the frequency close to the combined splitting $\Delta_1 + \Delta_2 = 75 \mu\text{eV}$ and accompanied by the quick relaxation between the levels E_4 and E_2 in Fig.1. The evolution is plotted vs time (upper scale) and the number of driving field periods (lower scale). All the other parameters are the same as in Fig.3. The stabilization of the flipped spin in the right QD can be observed due to the fast charge relaxation and slow spin relaxation.

is set at $\tau = 100 \text{ mK}$ being in agreement with the typical experimental conditions²². Such temperature corresponds to the thermal energy of about $8.75 \mu\text{eV}$ being lower than all the other energy parameters of the model, meaning that the thermal-induced jumps to the higher levels have low probability.

The most striking feature in Fig.4 is the observed spin flip stabilization, or spin flip locking in the right QD when the relaxation is introduced in combination with the interdot tunneling. This effect can be explained by comparing the fast charge relaxation with the slow spin relaxation and the resonant driving. Namely, the driving on the resonance $E_4 - E_1 = \omega$ excites the spin-flip transitions accompanied with the interdot tunneling from

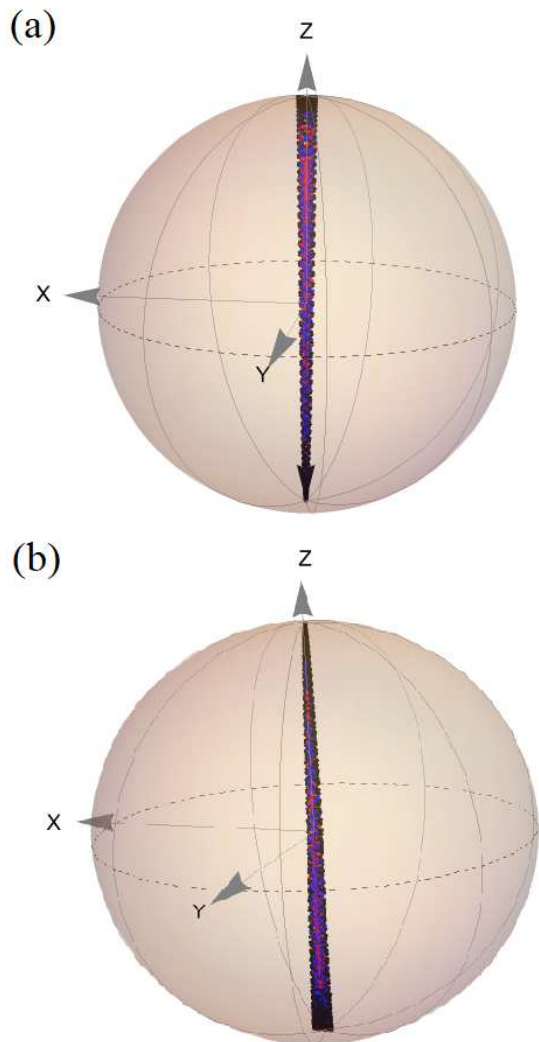


FIG. 5. Evolution of the vector (24) on the Bloch sphere for (a) the spin qubit and (b) the charge qubit. The initial state is on the south pole for both qubits. The type of the resonance and the parameters correspond to Fig.4. The final position of the vector (24) is on the north pole for the spin qubit in panel (a) and on the south pole for the charge qubit in panel (b).

right to the left QD. This is illustrated in Fig.6 where an example of the level occupancies $|C_n(t)|^2$ for the levels E_1, \dots, E_4 from Fig.1 is shown for the case of strong relaxation labeled by the red curve in Fig.4. The main purpose of Fig.6 is to show the evolution in the basis of the coordinate- and spin-resolved states of the static Hamiltonian (2) which is readily connected to the evolution of the mean values in Fig.4. In Fig.6 one can see that for the resonance between the levels E_1 and E_4 the off-resonance spin-up level E_2 occupation $|C_2(t)|^2$ monotonically grows with time until a certain saturation of the spin flip in the right QD is achieved. The spin-down level E_3 population $|C_3(t)|^2$ in the left QD demonstrates the slow-amplitude steady behavior while both of remaining

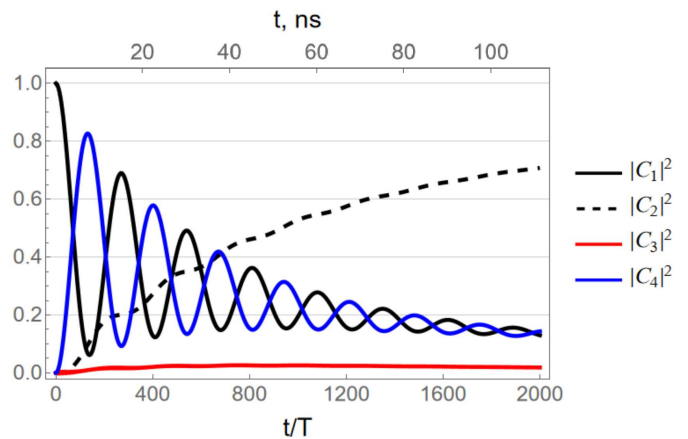


FIG. 6. An example of the level occupancies $|C_i(t)|^2$ evolution for the four-level subspace in Fig.1 is shown for the case of strong relaxation labeled by the red curves in Fig.4. The growing behavior of $|C_2(t)|^2$ describing the steady flipped spin in the right QD is explained as the combination of the resonant dynamics between the levels E_1 and E_4 accompanied by the fast charge relaxation between the levels E_4 and E_2 .

level populations $|C_1(t)|^2$ in the left QD and $|C_4(t)|^2$ in the right QD oscillate in resonance and demonstrate a decaying behavior. It is evident that a steady state in terms of the level populations is formed on longer times with the stable spin flip in the right QD. We would like to stress that the considered example of the dynamics in Fig.4 - Fig.6 demonstrates how useful the second (charge) qubit can be for the creation of the locked population of the excited state of the first (spin) qubit, finally leaving the second qubit in its ground state in the right QD.

We believe that the population behavior in Fig.6 and the associated spin and coordinate evolution in Fig.4 can be explained as the combination of the resonant dynamics between the levels E_1 and E_4 accompanied by the fast charge relaxation between the levels E_4 and E_2 . Indeed, from the upper E_4 level the fastest relaxation is the charge one, stimulating the transition to the level E_2 in the right QD but leaving the same flipped spin which holds for the sufficiently long time as it can be seen in Fig.4 and Fig.6. At longer times, when the spin relaxation stimulates the backward spin flip during the the transition to the ground level E_1 , the resonant driving field will trigger the described process once again. As a result, one can expect a quite long lifetime of the flipped spin in the same right QD where the electron has been initialized. Such steady state formation resulting into the spin polarization has been observed, for example, for the nuclear spins in double quantum dots^{59,60}, for the optically driven electron spin coupled to the bath of nuclear spins⁶¹, for the driven spin coupled to a bath of ultracold fermions⁶², and for the dynamics of two coupled qubits in the presence of the noise⁶³. This tunneling and relaxation- stabilized spin flip mechanism can be promising for spintronic applications.

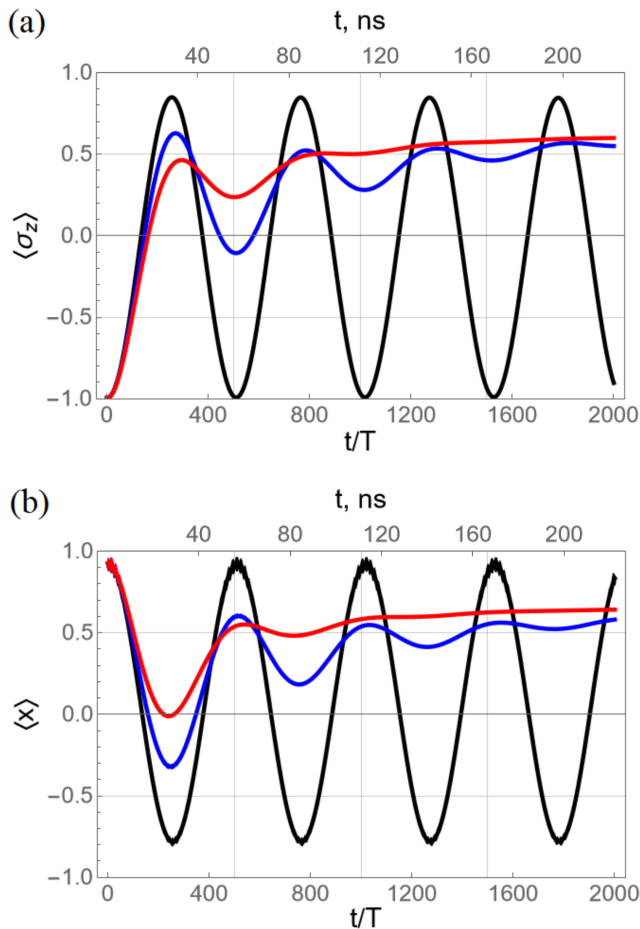


FIG. 7. The same as in Fig.4 for the second subharmonic $s = 2$ in (25) of the $E_1 - E_4$ resonant transition in Fig.1. The type of the resonance and the parameters (except the lower driving frequency and longer evolution time) are the same as in Fig.4. The relaxation leads to the dampening of the spin and coordinate oscillations and to the stabilization of the flipped spin.

C. Evolution on the second subharmonic

The relaxation effects become stronger for the EDSR subharmonics which frequency satisfies the condition

$$\omega_s = \frac{E_4 - E_1}{s}, \quad s = 2, 3, \dots \quad (25)$$

The reason is that the driving field on the subharmonics operates on lower frequencies and, as a result, the spin flip is achieved on longer times, being stronger affected by the relaxation. The driving frequency for the main harmonic of the $E_1 - E_4$ resonance for the considered Zeeman coupling and detuning is in the 18 GHz-range which may not be easily accessible. Hence, the driving on one of the the subharmonics (25) can be a viable option. We will consider the closest subharmonic $s = 2$. In Fig.7 we show the spin and coordinate evolution for

the second subharmonic $s = 2$ on the timescale of ~ 250 ns covering $2000 T$. All other parameters are the same as in Fig.4. As for the main harmonic, one can see that on the subharmonic the relaxation leads to the dampening of the spin and coordinate oscillations and to the stabilization of the flipped spin. A novel feature is that the stabilized flipped spin projection is somewhat higher for the cases with the relaxation (blue and red curves) compared to the respective coherent oscillations (black curve). We attribute this difference to the progressing effects of the charge and spin relaxation which come into play more quickly (measured in the driving field period) on the subharmonics due to the lower driving frequency, leading to the locking of the electron in the lowest state E_2 in the right QD with the flipped spin, compared to the state E_4 in the left QD. The predicted spin flip locking can be considered as an unexpectedly positive effect of the relaxation, maintaining the spin in the flipped state for sufficiently long time.

D. Spin flip amplitude dependence on the parameters

The predicted phenomenon of the locked flipped spin at the end of the evolution deserves a more detailed discussion. Namely, it is of interest to gather more information on the locked flipped spin amplitude as a function of the system parameters. First, we look at its dependence on the relaxation times which may vary depending on the structure type and quality. As before, we take equal energy and phase relaxation times for each qubit subsystem, $T_\varphi^{(2)} = T_e^{(2)} \equiv T^{(2)}$, $T_\varphi^{(1)} = T_e^{(1)} \equiv T^{(1)}$. In Fig.8 we plot the stabilized (i.e. obtained after a high number of driving periods) value of the spin projection $\langle \sigma_z \rangle_{t \rightarrow \infty}$ for different charge relaxation times $T^{(2)}$ labeled as differently shaped curves and covering a wide interval (0.01...0.15) μs which is consistent with the predictions for the GaAs-based double dots with the detuning¹². Each curve is plotted vs the ratio $T^{(2)}/T^{(1)}$ of the charge and spin relaxation time. All other parameters are the same as in Fig.4. This ratio is always lower than 1 since the spin relaxation in our system is significantly slower than the charge relaxation. The other parameters are for the main harmonic of the $E_1 - E_4$ resonance shown in Fig.4 and in Fig.6.

One can see in Fig.8 that for a long spin relaxation time $T^{(1)}$ when the ratio $T^{(2)}/T^{(1)}$ is small enough the locked spin flip amplitude approaches high values for any curve corresponding to the different charge relaxation time $T^{(2)}$. The highest amplitude of the flipped spin $\sigma_z^{\max} \sim 0.99$. We have already noted that the amplitude of the z spin projection is smaller than 1 in the presence of SOC so we believe that this result demonstrates the best available spin flip magnitude.

Another dependence of the final amplitude of the flipped spin is shown in Fig.9 as a function of the driving strength V_d . Different curves correspond to differ-

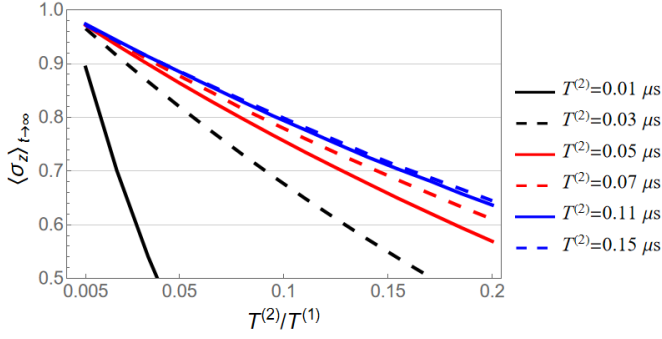


FIG. 8. Stabilized value of the spin projection $\langle \sigma_z \rangle_{t \rightarrow \infty}$ for different charge relaxation times $T^{(2)}$ labeled as differently shaped curves, each of them plotted vs the ratio $T^{(2)}/T^{(1)}$ of the charge and spin relaxation time. The other parameters are for the main harmonic of the $E_1 - E_4$ resonance shown in Fig.4 and in Fig.6. The high amplitude of the flipped spin $\sigma_z^{\max} \sim 0.99$ is achieved for moderate and high charge relaxation times $T^{(2)} > 0.03 \mu s$ and for the long spin relaxation time $T^{(1)}$ when $T^{(2)}/T^{(1)} < 0.05$.

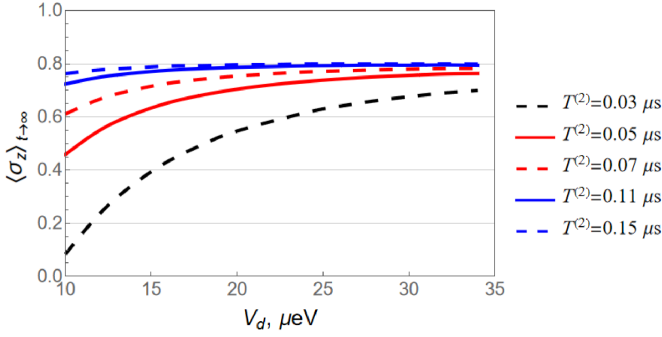


FIG. 9. Final value of the spin projection $\langle \sigma_z \rangle_{t \rightarrow \infty}$ as a function of the driving amplitude V_d for different values of charge relaxation time $T^{(2)}$. The ratio $T^{(2)}/T^{(1)} = 0.1$ and all other parameters are the same as in Fig.8. High amplitude of the locked flipped spin is achieved for the strong driving for all values of the charge relaxation time.

ent charge relaxation times $T^{(2)}$ with the fixed ratio $T^{(2)}/T^{(1)} = 0.1$ which is the typical value in the middle of Fig.8 from which all other parameters are kept. According to Fig.8, for such ratio $T^{(2)}/T^{(1)}$ the best achievable amplitude of $\langle \sigma_z \rangle_{t \rightarrow \infty}$ is about 0.8. It is evident from Fig.9 that it can be achieved for a wide range of the charge relaxation time $T^{(2)}$ where all of the curves in the right side of Fig.9 merge together.

Our final goal is to explore the dependence on the system parameters for the time when the stabilized spin flip amplitude is reached. In other words, we are interested to know not only how deep is the flip for the locked spin but also how fast this steady state can be reached. In Fig.10 we show the map of the spin flip stabilization time t_s in units of the driving period, shown vs the spin relaxation time $T^{(1)}$ and the driving amplitude V_d . We believe that these two parameters are the most

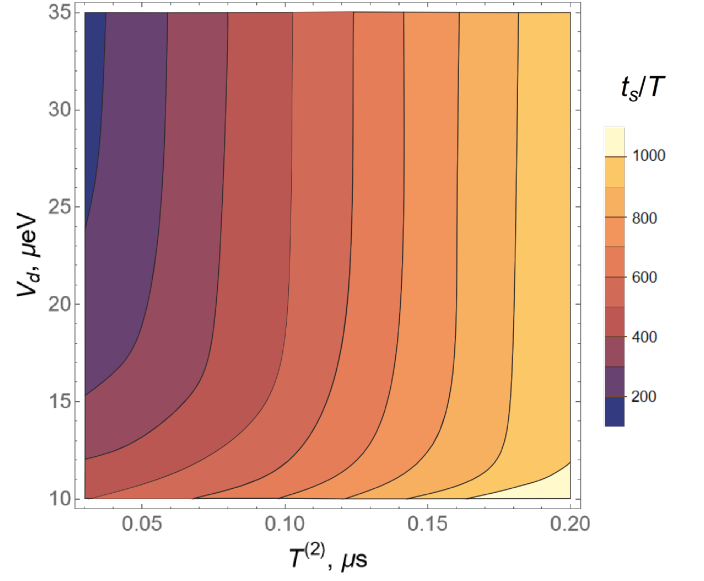


FIG. 10. Map of the spin flip stabilization time t_s/T in units of the driving period $T = 0.05 ns$ shown vs the spin relaxation time $T^{(1)}$ at fixed ratio $T^{(2)}/T^{(1)} = 0.1$ and vs the driving amplitude V_d . All other parameters are the same as in Fig.9. For a long spin relaxation time (right part of the map) the dependence of t_s/T on V_d is weak and is determined mainly by the relaxation time itself. At shorter relaxation time (left part of the map) the dependence on V_d is sharp, and the stabilized spin flip can be reached much faster.

crucial for determining the t_s . All other parameters are the same as in Fig.9 including the ratio $T^{(2)}/T^{(1)} = 0.1$. Each point corresponds to the evolution tracked on a high enough number of the driving field periods $T = 0.05 ns$ until the stabilized spin projection is achieved. One can see that for the slow relaxation corresponding to the long relaxation time at the right part of the map, the dependence of t_s/T is rather shallow, and the obtained times are quite long. This can be explained as a long and coherent-like evolution in the case of slow relaxation where many spin oscillations are visible until the transition to the steady state is manifested, as it can be seen for the examples shown in Fig.7 and Fig.4 by the black and blue curves. As for the area of the faster relaxation in Fig.10, at the left part of the map, the dependence on the driving amplitude V_d is much stronger, and the obtained stabilization time becomes significantly shorter if V_d is increased. This is due to the faster damping of the coherent spin oscillations which dissipate quickly, unmasking the strong dependence of the spin flip time (the inverse of the Rabi frequency) on the driving field amplitude. To summarize, for the fixed ratio $T^{(2)}/T^{(1)}$ we may interpolate the dependence of the t_s in Fig.10 by a simple formula $t_s \sim 1/\Omega_R + T^{(2)}$. It can be easily verified that this approximation describes a correct topology of the contour plot curves in Fig.10 if we remember that for the exact resonance the Rabi frequency Ω_R is proportional to the driving amplitude V_d . Another interesting feature

of the results in Fig.10 is that an increase in relaxation strength for the charge subsystem, i.e., the decreasing $T^{(2)}$ at a fixed ratio $T^{(2)}/T^{(1)} = 0.1$ for a long-lived spin state, can play a positive role here, providing the stabilized spin flip to be reached faster. The stabilized spin flip state can be reached on the interval of several hundreds driving periods which for the parameters in Fig.10 indicates the operation times of $15 \dots 60$ ns which is suitable for the information processing.

To conclude, the observed effect of the spin flip lock for different relaxation times and for different driving amplitudes indicates that this effect can be found in various double dot setups in the gate-defined quantum dots, which makes it promising for the applications in spintronics and quantum computations.

IV. CONCLUSIONS

We have studied the effects of relaxation on the spin and charge evolution in a driven double quantum dot modeling the spin and charge qubits interacting via the spin-orbit coupling. The relaxation effects have been included via the density matrix formalism. The numerical

analysis has demonstrated that the relaxation, leading to the trivial damping of the spin oscillations at the electric dipole spin resonance and its second subharmonic, plays a spin flip locking role for the multilevel dynamics where the spin flip is accompanied by an effective tunneling. The spin flip is found to be locked both on the main and on the neighboring subharmonic of the resonance, leading to the prolonged and stable spin flip in the desired quantum dot. The amplitude of the stabilized spin flip can reach as high as 0.99 in the presence of spin-orbit coupling for a wide range of the relaxation parameters. The stabilized spin flip state can be reached on the interval of about $15 \dots 60$ ns, making it suitable for the information processing. The predicted effect can be useful for the spin manipulation techniques in nanostructures and for the new coupled qubit proposals.

ACKNOWLEDGEMENTS

The authors are grateful to S.A. Studenikin, Yu.G. Makhlin, V.A. Burdov and A.A. Konakov for fruitful discussions. The authors are supported by the Ministry of Science and Higher Education of the Russian Federation through the State Assignment No FSWR-2023-0035.

* khomitsky@phys.unn.ru

- ¹ S.N. Shevchenko, S. Ashhab, and F. Nori, Phys. Rep. **492**, 1 (2010).
- ² O.V. Ivakhnenko, S.N. Shevchenko, F. Nori, Phys. Rep. **995**, 1 (2023).
- ³ Y.G. Semenov and K.W. Kim, Phys. Rev. B **75**, 195342 (2007).
- ⁴ J.M. Taylor, J.R. Petta, A.C. Johnson, A. Yacoby, C.M. Marcus, and M.D. Lukin, Phys. Rev. B **76**, 035315 (2007).
- ⁵ R. Sánchez, C. López-Monís, and G. Platero, Phys. Rev. B **77**, 165312 (2008).
- ⁶ K.D. Petersson, J.R. Petta, H. Lu and A.C. Gossard, Phys. Rev. Lett. **105**, 246804 (2010).
- ⁷ P. Nalbach, J. Knörzer, and S. Ludwig, Phys. Rev. B **87**, 165425 (2013).
- ⁸ H. Ribeiro, G. Burkard, J.R. Petta, H. Lu, and A.C. Gossard, Phys. Rev. Lett. **110**, 086804 (2013).
- ⁹ V. Srinivasa, K.C. Nowack, M. Shafei, L.M.K. Vandersypen, and J.M. Taylor, Phys. Rev. Lett. **110**, 196803 (2013).
- ¹⁰ F.R. Braakman, J. Danon, L.R. Schreiber, W. Wegscheider, and L.M.K. Vandersypen, Phys. Rev. B **89**, 075417 (2014).
- ¹¹ T. Nakajima, A. Noiri, J. Yoneda, M.R. Delbecq, P. Stano, T. Otsuka, K. Takeda, S. Amaha, G. Allison, K. Kawasaki, A. Ludwig, A.D. Wieck, D. Loss and S. Tarucha, Nature Nanotech. **14**, 555 (2019).
- ¹² J.A. Krzywda and Ł. Cywiński, Phys. Rev. B **104**, 075439 (2021).
- ¹³ D. Fernández-Fernández, J. Picó-Cortés, S. Vela Liñán and G. Platero, J. Phys.: Materials **6**, 034004 (2023).
- ¹⁴ H.-A. Engel and D. Loss, Phys. Rev. B **65**, 195321 (2002).

- ¹⁵ L.S. Levitov and E.I. Rashba, Phys. Rev. B **67**, 115324 (2003).
- ¹⁶ D. Stepanenko, N.E. Bonesteel, D.P. DiVincenzo, G. Burkard, D. Loss, Phys. Rev. B **68**, 115306 (2003).
- ¹⁷ S. Debald and C. Emary, Phys. Rev. Lett. **94**, 226803 (2005).
- ¹⁸ V.N. Golovach, M. Borhani, and D. Loss, Phys. Rev. B **74**, 165319 (2006).
- ¹⁹ N. Yokoshi, H. Imamura, and H. Kosaka, Phys. Rev. Lett. **103**, 046806 (2009).
- ²⁰ K.C. Nowack, F.H.L. Koppens, Yu.V. Nazarov, L.M.K. Vandersypen, Science **318**, 1430 (2007).
- ²¹ J. Stehlik, M.D. Schroer, M.Z. Maialle, M.H. Degani, and J.R. Petta, Phys. Rev. Lett. **112**, 227601 (2014).
- ²² A. Bogan, S. Studenikin, M. Korkusinski, L. Gaudreau, P. Zawadzki, A.S. Sachrajda, L. Tracy, J. Reno, and T. Hargett, Phys. Rev. Lett. **120**, 207701 (2018).
- ²³ S. Studenikin, M. Korkusinski, M. Takahashi, J. Ducautel, A. Padawer-Blatt, A. Bogan, D. G. Austing, L. Gaudreau, P. Zawadzki, A. Sachrajda, Y. Hirayama, L. Tracy, J. Reno, and T. Hargett, Communications Physics **2**, 159 (2019).
- ²⁴ V. Marton, A. Sachrajda, M. Korkusinski, A. Bogan, and S. Studenikin, Nanomat. **13**, 950 (2023).
- ²⁵ J.R. Petta, A.C. Johnson, J.M. Taylor, A. Yacoby, M.D. Lukin, C.M. Marcus, M.P. Hanson, and A.C. Gossard, Physica E **34**, 42 (2006).
- ²⁶ J. Kyriakidis and G. Burkard, Phys. Rev. B **75**, 115324 (2007).
- ²⁷ W.-M. Zhang, Y.-Z. Wu, C. Soo, and M. Feng, Phys. Rev. B **76**, 165311 (2007).
- ²⁸ G. Ramon and X. Hu, Phys. Rev. B **81**, 045304 (2010).

- ²⁹ K.D. Petersson, C.G. Smith, D. Anderson, P. Atkinson, G.A.C. Jones, and D.A. Ritchie, *Nano Lett.* **10**, 2789 (2010).
- ³⁰ R. Mizuta, R.M. Otxoa, A.C. Betz, and M.F. Gonzalez-Zalba, *Phys. Rev. B* **95**, 045414 (2017).
- ³¹ Y.-C. Yang, S.N. Coppersmith, and M. Friesen, *Phys. Rev. A* **100**, 022337 (2019).
- ³² A. Kregar and A. Ramšak, *Mod. Phys. Lett. B* **32**, 2040058 (2020).
- ³³ M.J. Rančić, *Phys. Rev. A* **105**, 032611 (2022).
- ³⁴ D. Fernández-Fernández, Y. Ban, and G. Platero, *Phys. Rev. Appl.* **18**, 054090 (2022).
- ³⁵ M. Pioro-Ladrière, Y. Tokura, T. Obata, T. Kubo, and S. Tarucha, *Appl. Phys. Lett.* **90**, 024105 (2007).
- ³⁶ J.H. Bodey, R. Stockill, E.V. Denning, D.A. Gangloff, G. Éthier-Majcher, D.M. Jackson, E. Clarke, M. Hugues, C. Le Gall and M. Atatüre, *NPJ Quantum Information* **95**, 1 (2019).
- ³⁷ D.V. Khomitsky and S.A. Studenikin, *Phys. Rev. B* **106**, 195414 (2022).
- ³⁸ D.V. Khomitsky, M.V. Bastrakova, V.O. Munyaev, N.A. Zaprudnov, and S.A. Studenikin, *Phys. Rev. B* **108**, 205404 (2023).
- ³⁹ H.-P. Breuer and F. Petruccione, *The theory of open quantum systems*, Oxford University Press (New York), 2003.
- ⁴⁰ S. Kohler, T. Dittrich, and P. Hänggi, *Phys. Rev. E* **55**, 300 (1997).
- ⁴¹ M. Grifoni, P. Hänggi, *Phys. Rep.* **304**, 229 (1998).
- ⁴² D.W. Hone, R. Ketzmerick, and W. Kohn, *Phys. Rev. E* **79**, 051129 (2009).
- ⁴³ P. Nalbach and M. Thorwart, *Phys. Rev. Lett.* **103**, 220401 (2009).
- ⁴⁴ C. Xu, A. Poudel, and M.G. Vavilov, *Phys. Rev. A* **89**, 052102 (2014).
- ⁴⁵ Y. Makhlin, G. Schön, and A. Shnirman, *Rev. Mod. Phys.* **73**, 357 (2001).
- ⁴⁶ A.M. Satanin, M.V. Denisenko, S. Ashhab, and F. Nori, *Phys. Rev. B* **85**, 184524 (2012).
- ⁴⁷ V.O. Munyaev and M.V. Bastrakova, *Phys. Rev. A* **104**, 012613 (2021).
- ⁴⁸ D.S. Pashin, P.V. Pikunov, M.V. Bastrakova, A.E. Schegolev, N.V. Klenov, I.I. Soloviev, *Beilstein J. of Nanotechnol.* **14**, 1116 (2023).
- ⁴⁹ M. Bonifacio, D. Domínguez, and M.J. Sánchez, *Phys. Rev. B* **101**, 245415 (2020).
- ⁵⁰ M. Tokman, A. Behne, B. Torres, M. Erukhimova, Y. Wang, and A. Belyanin, *Phys. Rev. A* **107**, 013721 (2023).
- ⁵¹ B. Marques, A.A. Matoso, W.M. Pimenta, A.J. Gutiérrez-Esparza, M.F. Santos and S. Pádua, *Sci. Rep.* **5**, 16049 (2015).
- ⁵² L. Zhang, L. Wang, M.F. Gelin, and Y. Zhao, *J. Chem Phys.* **158**, 204115 (2023).
- ⁵³ J. Evers, *J. Mod. Opt.* **52**, 2699 (2005).
- ⁵⁴ E. Ilinova and A. Derevianko, *Phys. Rev. A* **86**, 013423 (2012).
- ⁵⁵ B. Boukhris, A. Tirbiyine, and J. El Qars, *Mod. Phys. Lett. B* **37**(35), 2350194 (2023).
- ⁵⁶ P.P. Hofer, M. Perarnau-Llobet, L.D.M. Miranda, G. Haack, R. Silva, J. Bohr Brask, and N. Brunner, *New J. Phys.* **19**, 123037 (2017).
- ⁵⁷ M. Cattaneo, G.L. Giorgi, S. Maniscalco, and R. Zambrini, *New J. Phys.* **21**, 113045 (2019).
- ⁵⁸ T. Albash, S. Boixo, D.A. Lidar, P. Zanardi, *New J Phys.* **14**, 123016 (2012).
- ⁵⁹ J.R. Petta, J.M. Taylor, A.C. Johnson, A. Yacoby, M.D. Lukin, C.M. Marcus, M.P. Hanson, and A.C. Gossard, *Phys. Rev. Lett.* **100**, 067601 (2008).
- ⁶⁰ M.J.A. Schuetz, E.M. Kessler, L.M.K. Vandersypen, J.I. Cirac, and G. Giedke, *Phys. Rev. B* **89**, 195310 (2014).
- ⁶¹ A. Vezvae, G. Sharma, S.E. Economou, and E. Barnes, *Phys. Rev. B* **103**, 235301 (2021).
- ⁶² M. Knap, D.A. Abanin, and E. Demler, *Phys. Rev. Lett.* **111**, 265302 (2013).
- ⁶³ S. Das Sarma, R.E. Throckmorton, and Y.-L. Wu, *Phys. Rev. B* **94**, 045435 (2016).